



CHORUS

This is the accepted manuscript made available via CHORUS. The article has been published as:

Intrinsic ductility of random substitutional alloys from nonlinear elasticity theory

I. S. Winter, M. de Jong, J. Montoya, E. Rothchild, and D. C. Chrzan

Phys. Rev. Materials **3**, 113608 — Published 27 November 2019

DOI: [10.1103/PhysRevMaterials.3.113608](https://doi.org/10.1103/PhysRevMaterials.3.113608)

Intrinsic Ductility of Random Substitutional Alloys from Nonlinear Elasticity Theory

I. S. Winter,^{1,2,3,*} M. de Jong,^{1,4} J. Montoya,² E. Rothchild,¹ and D. C. Chrzan^{1,5,†}

¹*Department of Materials Science and Engineering,
University of California, Berkeley, California 94720, USA*

²*Energy Technologies Area, Lawrence Berkeley
National Laboratory, Berkeley, California, 94720, USA*

³*Lawrence Livermore National Laboratory,
Livermore, California, 94550, USA*

⁴*SpaceX, 1 Rocket Road, Hawthorne, CA 90250, USA*

⁵*Materials Sciences Division, Lawrence Berkeley
National Laboratory, Berkeley, California, 94720, USA*

Abstract

A method suitable for computing the ideal strength of random substitutional alloys is introduced. The method relies on nonlinear continuum elasticity theory, and allows for the high throughput computation of ideal strength. The method also allows for the high throughput computation of an intrinsic ductility parameter defined for a given applied stress state as the ratio of the strain associated with the cleavage instability to the strain associated with the first shear instability. The intrinsic ductility parameter is shown to correlate well with the measured elongations to failure for elemental body-centered-cubic and hexagonal close-packed metals. Application to four high entropy alloys indicate that the intrinsic ductility parameter describes their experimental compressions to failure well. The method is used to argue that the brittle refractory high entropy alloy Ta-Nb-V-W-Mo could be made much more ductile through replacement of Mo with Nb. The potential for the high throughput optimization of high entropy and chemically complex alloys is discussed.

I. INTRODUCTION

The ideal strength (IS) provides the theoretical upper limit to the strength of a material and is one of the few mechanical properties that can be calculated easily using first-principles methods¹⁻³ as well as measured experimentally.⁴⁻⁸ While a perfectly crystalline material does not exist in any engineering application, ideal strength calculations have been shown to be useful in numerous areas: IS has been applied to understanding the homogeneous nucleation of dislocations under nanoindentation,⁹⁻¹¹ the intrinsic ductility of a crystal (the preference of a crystal to undergo a shear instability under a tensile load)¹²⁻¹⁴ and the preferred cleavage plane of transition metal aluminides.¹⁵ Perhaps most famously, Frenkel's simple ideal strength model¹⁶ helped lead to the theory of defect-mediated plasticity.¹⁷⁻¹⁹ Wang and Li have used ideal strength calculations to connect the correlation length of atomic motion with the strength of bulk metallic glasses.²⁰ While defect-mediated plasticity is the predominant deformation mechanism in structural alloys, it is becoming clear that IS can play an integral role in understanding certain aspects of the mechanical properties of structural materials.

Compositionally complex alloys, i.e. those without a single dominant base-element, including high entropy alloys (HEAs), have generated much enthusiasm in the field of metallurgy over the past decade.²¹⁻²⁴ For example, many HEAs have been developed with interesting properties including high wear-resistance,²⁵ high-temperature strength,²⁶ and a combination of high strength and ductility.²⁷ These remarkable properties can be engineered into HEAs because the design space for these alloys is very large.^{28,29} At the same time, however, the size of the design space poses challenges for alloy designers: How does one rapidly identify useful alloys to synthesize, and once synthesized, how can the properties of the alloy be optimized?

Miracle *et al.* developed an approach to exploring this large phase space that incorporates empirical rules for alloy design regarding density, computational analysis of phase stability using CALPHAD, and high throughput experiments to identify alloys with promising properties.²⁹ Singh *et al.* used the coherent potential approximation (CPA) and density functional theory (DFT) to compute the relative phase stability and elastic constants of complex solid-solution alloys.³⁰ Singh *et al.* stop short of predicting the mechanical properties of the alloys using CPA, and instead, use empirical interatomic potentials and quasistatic

loading conditions within a molecular dynamics simulation to assess the relative ductility of the alloys. This analysis, of course, requires the development of suitable interatomic potentials, and these potentials introduce substantial uncertainty into the conclusions. So while phase stability is becoming more accessible to DFT-based methods, the assessment of the ductility of the stable alloys using DFT, particularly in a high-throughput computing context, remains as a ongoing theoretical challenge.

In what follows, an easily computed parameter that is shown to correlate well with experimental measurements of elongation to fracture of body-centered cubic (BCC) and hexagonal close-packed (HCP) metals is introduced. The parameter, dubbed the intrinsic ductility parameter, is derived from IS calculations, and is similar to the previously defined brittleness parameter of the alloy,³¹ but more convenient to compute, particularly for compositionally complex alloys.

While IS calculations for elemental or ordered crystals can be performed with relative ease, the calculation of the IS of a random solid solution (including HEAs and compositionally complex alloys) using DFT continues to be problematic for several reasons. Perhaps most importantly, IS calculations rely on crystalline symmetry. However, random solid solution alloys are crystalline only in an average sense. The implication is that most supercells suitable for first principles based calculations will not have a crystalline symmetry equivalent to the average symmetry of the alloy, and this confounds computation of IS. To circumvent this difficulty, previous studies have used methods such as the virtual crystal approximation (VCA)³² or coherent potential approximation (CPA)^{33,34} to compute the ideal strength of solid solutions. These approaches provide substantial insight. However, each has its limitations. For example, VCA is only applicable when very similar atoms are involved in the alloy. CPA is more broadly applicable, but typically requires the use of basis states more complicated than plane waves, and thus is not compatible with the most commonly available DFT codes.

In the following, a method for computing IS of random substitutional alloys that is rooted in nonlinear continuum elasticity theory is introduced. The method enables exploration of all applied stress states, direct investigation of elastic stability at both infinitesimal and small, but finite, strains, and is easily employed with any modern electronic structure method, including CPA. The method also enables the definition of an intrinsic ductility parameter that can be used to discover and optimize ductile chemically complex alloys. The method is

applied to elemental body centered cubic (BCC) and hexagonal close packed (HCP) metals where it is demonstrated that experimentally measured elongations vary systematically and monotonically with the intrinsic ductility parameter. Application to four HEAs (in which every component appears with the same concentration): Hf-Zr-Ti-Nb-V, Ta-Nb-V-W-Mo, Ta-Nb-V-W, and Ti-Ta-Nb-V, shows that the method works in more complicated systems as well. Finally, the method is used to argue that ductility of Ta-Nb-V-W-Mo can be improved substantially by replacing Mo with Nb.

II. METHOD

A. Elastic Stability

Begin by noting that the symmetric Wallace tensor (SWT), $\mathbf{\Lambda}$, that governs the elastic stability of an anisotropic solid, is^{35,36}

$$\Lambda_{klmn} = C'_{klmn} + \frac{1}{2} (\tau_{km}\delta_{ln} + \tau_{kn}\delta_{lm} + \tau_{lm}\delta_{kn} + \tau_{ln}\delta_{km} - \tau_{kl}\delta_{mn} - \tau_{mn}\delta_{kl}). \quad (1)$$

Here δ_{ln} is the Kronecker-delta function, τ_{km} the Second Piola-Kirchhoff stress tensor, and C'_{klmn} the second-order elastic constants of the solid under finite deformation (ECFD). C'_{klmn} is defined:

$$C'_{klmn} = \frac{1}{V(\boldsymbol{\eta})} \left(\frac{\partial^2 E}{\partial \beta_{kl} \partial \beta_{mn}} \right)_{\boldsymbol{\eta}}, \quad (2)$$

with $V(\boldsymbol{\eta})$ being the volume at a finite (Lagrangian) strain ($\boldsymbol{\eta}$), E the elastic energy, and $\boldsymbol{\beta}$ an infinitesimal strain applied in addition to the finite strain. A material is elastically unstable if $\det \mathbf{\Lambda} \leq 0$, and is said to be intrinsically ductile if under an applied uniaxial load the eigenstrain associated with the instability breaks the symmetry of the crystal in the current strain state; the material fails in a manner other than the Young's modulus along the loading direction going to zero.

The elastic energy at an unstrained volume (V_0) is approximated using a Taylor series expansion up to the third order in Lagrangian strain. (It should be noted, however, that this method can be generalized to any order.)

$$\Delta E \approx \frac{1}{2!} C_{klmn} \eta_{kl} \eta_{mn} + \frac{1}{3!} C_{klmnpq} \eta_{kl} \eta_{mn} \eta_{pq} + \dots, \quad (3)$$

with the second- and third-order elastic constants (SOECs and TOECs) defined as

$$C_{klmn} = \frac{1}{V_0} \left(\frac{\partial^2 E}{\partial \eta_{kl} \partial \eta_{mn}} \right)_{\eta=0}, \quad (4a)$$

$$C_{klmnpq} = \frac{1}{V_0} \left(\frac{\partial^3 E}{\partial \eta_{kl} \partial \eta_{mn} \partial \eta_{pq}} \right)_{\eta=0}. \quad (4b)$$

By combining equations (2) and (3)³⁷ ECFD can be determined entirely in terms of the elastic constants at zero strain and the (presumed known) finite strain.

B. Derivation of Elastic Constants under Finite Deformation

Three configurations are considered in deriving the ECFD: the zero strain reference configuration (\mathbf{X}), configuration under a finite strain of $\boldsymbol{\eta}(\mathbf{x})$, and a configuration under a combined finite and infinitesimal strain ($\bar{\mathbf{x}}$), see FIG. 1 for a graphical representation. These configurations can be mapped to each other by the use of deformation gradients, which are defined as

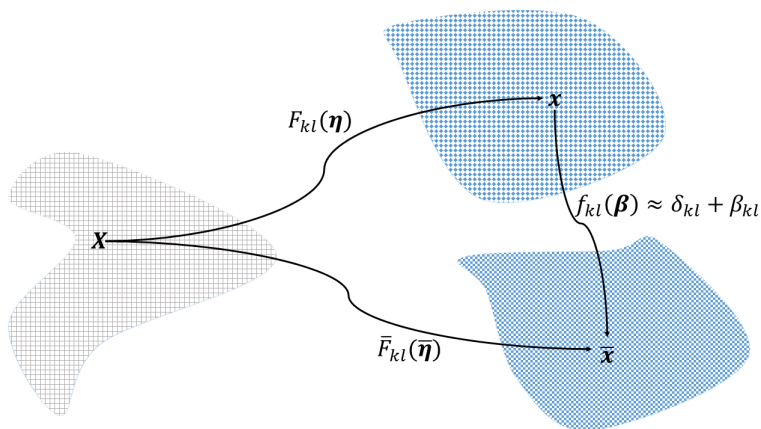


FIG. 1. Illustration of the three strain states considered in the derivation of C'_{klmn} . \mathbf{F} is the deformation gradient mapping the reference configuration (\mathbf{X}) to the finite strain state (\mathbf{x}). $\bar{\mathbf{F}}$ is the deformation gradient mapping \mathbf{X} to the configuration ($\bar{\mathbf{x}}$) associated with the combined finite and infinitesimal strain. \mathbf{f} maps \mathbf{x} to $\bar{\mathbf{x}}$, which is under a combined finite and infinitesimal strain.

$$F_{km} = \frac{\partial x_k}{\partial X_m}, \quad (5a)$$

$$\bar{F}_{km} = \frac{\partial \bar{x}_k}{\partial X_m}, \quad (5b)$$

$$f_{km} = \frac{\partial \bar{x}_k}{\partial x_m}. \quad (5c)$$

The deformation gradient is related to the Lagrangian strain by

$$\eta_{km} = \frac{1}{2} (F_{pk}F_{pm} - \delta_{km}), \quad (6)$$

and can be solved for analytically entirely in terms of the strain. Due to the definition of the Lagrangian strain in equation (14) (see Appendix A) it can be shown that there is no one-to-one mapping between \mathbf{F} and $\boldsymbol{\eta}$. This is due to the fact that $\boldsymbol{\eta}$ is not affected by any rotations of \mathbf{F} . As a result, \mathbf{F} can be assumed to be upper-triangular, which enables one to write $\mathbf{F} = \mathbf{F}(\boldsymbol{\eta})$ directly by solving for \mathbf{F} in terms of $\boldsymbol{\eta}$ using equation (14).

With $\mathbf{F} = \mathbf{F}(\boldsymbol{\eta})$ in hand we can define all configurations in terms of the applied strains³⁸ using equation (5) and assuming that \mathbf{f} can be expressed in terms of the infinitesimal strain ($\boldsymbol{\beta}$) as

$$f_{km} = \delta_{km} + \beta_{km}. \quad (7)$$

By substituting the Taylor series expansion of the elastic energy in terms of the combined infinitesimal and finite strain state ($\bar{\boldsymbol{\eta}}$) into the definition of the ECFD, C'_{klmn} , and then evaluating the equation at $\bar{\boldsymbol{\eta}}$. C'_{klmn} is expressed as

$$C'_{ijkl} = \frac{1}{J(\boldsymbol{\eta})} \left[(C_{mnpq} + C_{mnpqrs}\eta_{rs}) \left(\frac{\partial \bar{\eta}_{mn}}{\partial \beta_{kl}} \frac{\partial \bar{\eta}_{pq}}{\partial \beta_{ij}} \right)_{\bar{\boldsymbol{\eta}}=\boldsymbol{\eta}} + \left(C_{mnpq} + \frac{1}{2}C_{mnpqrs}\eta_{rs} \right) \left(\frac{\partial^2 \bar{\eta}_{mn}}{\partial \beta_{ij} \partial \beta_{kl}} \right)_{\bar{\boldsymbol{\eta}}=\boldsymbol{\eta}} \eta_{pq} \right], \quad (8)$$

where $J(\boldsymbol{\eta}) = \det \mathbf{F}$. It should be noted that equation (8) is similar to that determined by Wang and Li³⁷, but includes the term $\frac{\partial^2 \bar{\eta}_{mn}}{\partial \beta_{ij} \partial \beta_{kl}} \bar{\eta}_{pq}$. As $\bar{\mathbf{F}}$ can be determined entirely in terms of $\boldsymbol{\eta}$ and $\boldsymbol{\beta}$, equation (8) is completely defined in term of $\boldsymbol{\eta}$ and the elastic constants. A derivation of $\left(\frac{\partial \bar{\eta}_{mn}}{\partial \beta_{ij}} \right)_{\bar{\boldsymbol{\eta}}=\boldsymbol{\eta}}$ and $\left(\frac{\partial^2 \bar{\eta}_{mn}}{\partial \beta_{ij} \partial \beta_{kl}} \right)_{\bar{\boldsymbol{\eta}}=\boldsymbol{\eta}}$ can be found in VIA.

For the on-average body-centered-cubic (BCC) materials considered in this work, ideal tensile strength calculations are performed along the $\langle 001 \rangle$ direction. This orientation is

considered due to the fact that it is considered to be the weakest orientation in BCC and links between these calculations and fracture behavior of BCC crystals have been demonstrated.^{12–14,39–44}

For a uniaxial load applied along the [001] direction ECFD are:⁴⁴

$$C'_{11} = C_{11} + (3C_{11} + C_{12} + C_{111} + C_{112})\zeta + (-C_{11} + C_{12} + C_{112})\xi, \quad (9a)$$

$$C'_{12} = C_{12} + (2C_{12} + 2C_{112})\zeta + (-C_{12} + C_{123})\xi, \quad (9b)$$

$$C'_{13} = C_{12} + (C_{112} + C_{123})\zeta + (C_{12} + C_{112})\xi, \quad (9c)$$

$$C'_{33} = C_{11} + (-2C_{11} + 2C_{12} + 2C_{112})\zeta + (4C_{11} + C_{111})\xi, \quad (9d)$$

$$C'_{44} = C_{44} + \frac{1}{4}(C_{11} + 3C_{12} + 4C_{144} + 4C_{166})\zeta + \frac{1}{4}(C_{11} + C_{12} + 4C_{44} + 4C_{166})\xi, \quad (9e)$$

$$C'_{66} = C_{44} + \frac{1}{2}(C_{11} + C_{12} + 4C_{44} + 4C_{166})\zeta + \frac{1}{2}(C_{12} - 2C_{44} + 2C_{144})\xi. \quad (9f)$$

Here ζ and ξ are components of the Lagrangian strain tensor such that the tensor has the form in Voigt notation $\boldsymbol{\eta} = (\zeta, \zeta, \xi, 0, 0, 0)$. Using the expansion of $\boldsymbol{\tau}$ in terms of $\boldsymbol{\eta}$ and knowing that $\tau_{11} = 0$ for a uniaxial load applied along [001], both $\boldsymbol{\eta}$ and $\boldsymbol{\tau}$ can be defined entirely by ξ .⁴⁴ It should be noted that the strain range at which equation (9) remains valid has not been specifically tested in this work. Instead, it is assumed that the equation is valid for the strains considered in this work (unless otherwise stated), and the predictions are then analyzed. The estimate of the strain ranges over which equation (9) is valid can be tested following an approach similar to that introduced by Tromp *et al.*⁴⁵

The approach also allows identification of an intrinsic ductility parameter, χ , defined using SWT. Specifically, one computes the eigenvalues of SWT as a function of uniaxial strain along the elastically softest direction of the crystal. The crystal becomes elastically unstable when one of these eigenvalues, λ , becomes equal to zero. This event marks elastic instability for the crystal, and the Lagrangian strain at which this happens is defined to be ξ . Continuing to strain the crystal along the initial strain path, one often finds that additional eigenvalues of SWT may go to zero at their respective finite strains. Given this list of imposed strains and eigenvalues one can characterize the type of elastic instability associated with each by examining the eigenstrain of the SWT corresponding to each of the eigenvalues. These eigenstrains represent the local infinitesimal strain about the crystal in its macroscopically strained state. Eigenstrains that leave the symmetry of the crystal

unaltered from that associated with the strain path are associated with cleavage. Those that result in a symmetry change for the strained crystal are deemed to be shear failure modes. After the eigenstrains of the unstable modes are categorized, the intrinsic ductility parameter, χ , can be defined as:

$$\chi = \frac{\xi_C}{\xi_S}, \quad (10)$$

where ξ_C is the strain associated with the first cleavage mode that becomes unstable, and ξ_S is the strain associated with the first shear mode to become unstable. It is apparent how this parameter can be related to crack propagation: a shear instability at the crack tip would prevent further cleavage and possibly lead to the nucleation of dislocations. Thus, the further the shear and cleavage instabilities are apart, the more likely that a shear or cleavage event should occur, assuming the cleavage instability occurs at larger strains.

Our formalism has been implemented in the elasticity analysis module of the open-source pymatgen⁴⁶ software package. Given the second and third-order elastic constants for a given material, the SWT, eigenstrain profile (e. g. in 4), and intrinsic ductility parameter as defined above may all be determined. Previously reported⁴⁷ values for the DFT-calculated third-order elastic constants have also been made available via the Materials Project API⁴⁸.

C. Intrinsic Ductility for Alloys

This formalism allows for SWT to be efficiently approximated for a solid solution. One can do this by calculating the SOECs and TOECs⁴⁴ of a special quasi-random structure (SQS).^{49,50} These SQS cells typically display triclinic symmetry. The elastic constants for these cells are computed using the methods in references,^{44,51} and then symmetrized to match the point group of the macroscopic crystal using

$$C_{klmn} = \frac{1}{n_G} \sum_{\alpha=1}^{n_G} a_{kp}^{(\alpha)} a_{lq}^{(\alpha)} a_{mr}^{(\alpha)} a_{ns}^{(\alpha)} C_{pqrs}^{SQS}, \quad (11a)$$

$$C_{klmnpq} = \frac{1}{n_G} \sum_{\alpha=1}^{n_G} a_{kr}^{(\alpha)} a_{ls}^{(\alpha)} a_{mt}^{(\alpha)} a_{nu}^{(\alpha)} a_{pv}^{(\alpha)} a_{qw}^{(\alpha)} C_{rstuvw}^{SQS}, \quad (11b)$$

with n_G being the number of elements in the point group and Einstein summation notation implied for all Latin subscripts. The $a_{ij}^{(\alpha)}$'s are the matrix elements of the transformation matrix linking the transformed coordinate system to the original coordinate system by the

crystalline point group operation α . The solid solution can be better approximated for a given property by doing a weighted average over several SQS using the small set of ordered structures method (SSOS).⁵² In this method the predicted value for a general material property (f) of an alloy can be expressed as

$$\langle f \rangle \approx \sum_{\gamma=1}^{n_{SQS}} w_{\gamma} f(\sigma_{\gamma}^{SQS}), \quad (12)$$

with σ_{γ}^{SQS} being the configuration of the γ^{th} SQS structure and w_{γ} being the weight for the γ^{th} configuration. The final elastic constants are found by performing a weighted averaging of the highest performing SQS structures (those with correlations that best match a random alloy).

Pair correlation functions are considered, which correspond to a cut-off distance r of $r < 1.7a_0$, where a_0 represents the lattice constant of the BCC conventional cell. In addition, triplet correlation functions are used. These are selected such that no triplets contain pairs longer than $1.42a_0$. The atomic correlation functions of a large collections of SQS cells are computed using the alloy theoretic automated toolkit (ATAT)^{53–55}. The weights associated with each SQS structure used in eqn. (12) are shown in TABLE I. For information on the SSOS cells generated see VID.

TABLE I. List of the weights used in SSOS average for alloys as shown in eqn. (12). The weights used for the 5-component equiatomic system are those used for Hf-Zr-Ti-Nb-V and Ta-Nb-V-W-Mo, and were taken from reference⁵². The weights for the 4-component equiatomic system are those used for Ta-Nb-V-W and Ti-Ta-Nb-V.

System	w_1	w_2	w_3	w_4
5 components ⁵²	0.200	0.400	0.400	
4 components	0.108	0.408	0.373	0.111
Ta _{0.2} Nb _{0.4} V _{0.2} W _{0.2}	0.150	0.296	0.390	0.164

III. RESULTS

A. Second Order Elastic Constants

Experimental studies have examined the compressive stress-strain curves of four HEAs of interest: Hf-Zr-Ti-Nb-V, Ta-Nb-V-W-Mo, Ti-Ta-Nb-V, and Ta-Nb-V-W. Hf-Zr-Ti-Nb-V values for compression to fracture at room temperature are found to be 30% engineering strain (ES),⁵⁶ while this number for Ta-Nb-V-W-Mo is approximately 1.7% ES.²⁶ In the case of Ti-Ta-Nb-V and Ta-Nb-V-W the measured compression to failures are greater than 40% and 14% strain respectively.⁵⁷ It is of interest then to see if the method discussed in this paper agrees in general with these experimental findings. As a first step and test of the SSOS method, the poly-crystalline elastic constants of Hf-Zr-Ti-Nb-V and Ta-Nb-V-W-Mo are compared between SSOS, CPA, and experiment. The SSOS and their weights used for the equiatomic HEAs were the same as those used by Jiang and Uberuaga.⁵² In the case of SSOS, the isotropic elastic constants are estimated using self-consistent bounds.⁵⁸⁻⁶¹ SSOS and CPA isotropic elastic constants appear to be in good agreement (see Table II). This result is not altogether surprising considering previous works comparing SQS and CPA found good agreement between the two methods when calculating elastic constants.⁶²⁻⁶⁴ The difference in Young’s modulus between the theoretical approaches and experiment could be in part explained by the presence of a second phase present in the Hf-Zr-Ti-Nb-V samples used for measuring Young’s modulus.⁵⁶

TABLE II. Poly-crystalline elastic constants computed using SSOS compared to CPA and theory. All units are in GPa. In the case of SSOS the isotropic Young’s modulus was calculated using self-consistent bounds.⁵⁸⁻⁶¹

HEA	Y_{SSOS}	Y_{CPA}	Y_{Exp}	G_{SSOS}	G_{CPA}
Hf-Zr-Ti-Nb-V	93.4	97.1 ³⁴	128 ⁵⁶	34.2	35.0 ³⁴
Ta-Nb-V-W-Mo	185		180 ²⁶	67.7	

B. Intrinsic Ductility of Elements

Consider first the value of χ (calculated using SOECs and TOECs from DFT^{44,47}) for BCC and HCP elemental metals. Figure 2 plots the computed value of χ vs. typical experimentally measured elongations to failure of 16 elemental metals. Often, the experimentally measured elongations to failure are reported within a range, as these can depend on microstructure, purity, etc. In these cases, the midpoint of the reported range of elongation is used for the analysis. Empirically, the correlation can be represented by the red dashed line in Fig. 2. The Pearson and Spearman correlation coefficients are both 0.84. This result is particularly promising, as the Spearman correlation is quite strong, suggesting that the ordering predicted by χ is robust. The implication is that χ can be used to predict the effects of alloying additions or compositional changes on the ductility of a specific alloy. The strong correlation is somewhat unexpected considering the great complexity of plasticity in metals. Elongation is determined by mechanisms operating on length scales on the order of ångströms to millimeters, and yet its value is highly correlated with a simple analytical elasticity model, the inputs of which can be obtained from first principles. Note that χ differs from the brittleness parameter defined by Ogata et al.^{31,65} which they applied to a different set of materials. However, the level of correlation between experimentally measured elongations and χ is comparable to that between the brittleness parameter of reference³¹ and measured fracture toughness's.

To check the sensitivity of the χ parameter to changes in the elastic constants all SOECs and TOECs for each system were allowed to vary by 20% of the reported values. χ was then calculated 1000 times using elastic constants randomly assigned within the specified error range. The error in χ for each system was taken to be the standard deviation of the 1000 χ values. In viewing the results the error in χ shown in Table V it is clear that higher values of χ tend to have higher associated errors.

To ascertain the spread in the correlation between the experimentally-measured elongation to fracture and χ , the average of the range of elongation to fracture for each element and χ were fit to a line. From this linear statistical model the predicted 95% confidence interval was estimated and is shown in Table IV. Assuming that the the data shown in Fig. 2 can be fit to a linear statistical model (using Mathematica's statistical model analysis tools⁷¹) the predicted 95% confidence interval was estimated. For almost all elements con-

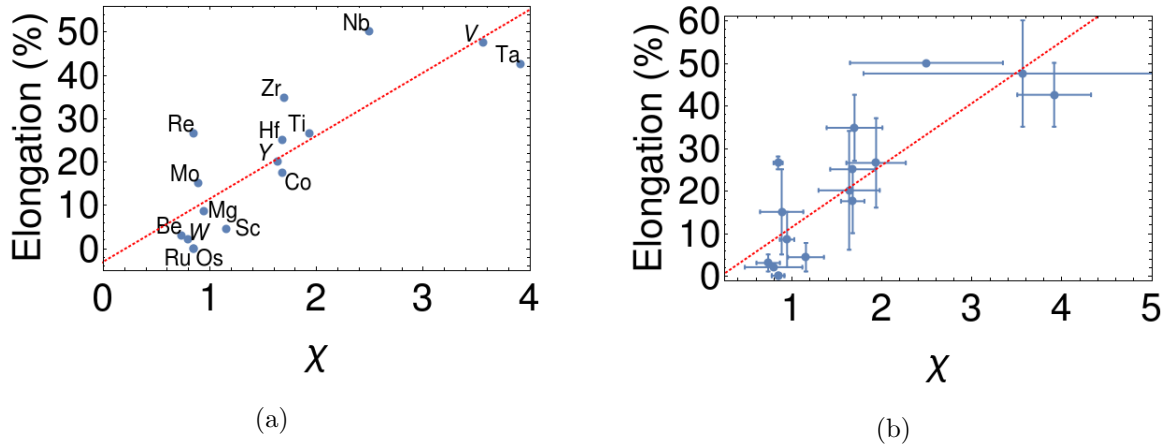


FIG. 2. Comparison of the calculated intrinsic ductility χ and an average of experimental values of elongation to fracture at room temperature for commercially pure metals^{66–70}. The SOECs and TOECs of all elements used in the calculation of χ were taken from reference⁴⁴ with the exception of V, which was taken from Winter *et al.*⁴⁷. Fig. a contains the plot without error bars, but with labels of the plot, while Fig. b is the same plot, but includes error bars.

sidered the predicted confidence interval is approximately 10 – 15% elongation to failure. While this number is large enough to make quantitative predictions of elongation inaccessible, the ability to qualitatively estimate a material’s ductility could have significant impacts on structural materials design. Further, it appears that this qualitative correlation between elongation to fracture and χ remains intact even when errors as large as 20% in the elastic constants are introduced.

To better evaluate the ability of the χ parameter to assess elongation to fracture, the Pearson and Spearman correlation between χ and experimentally measured elongation to fracture was compared to the correlation between the Pugh ratio (the ratio of the isotropic bulk modulus and shear modulus, or B/G)⁶⁹ and elongation to fracture, which is plotted in Fig. 3. The Pugh ratio was computed using the same SOECs that were employed in the calculation of χ shown in Table V. B and G were then estimated using self-consistent bounds^{58–61}. The Pugh ratio correlates with the elongations to fracture with Pearson and Spearman correlation coefficients of 0.84 and 0.76 respectively, which is less than for χ in the case of Spearman correlation.

TABLE III. List of experimental values of elongation to fracture and their references as well as the χ parameter computed with nonlinear elasticity theory and an estimate of the χ parameter’s error.

System	Elongation (%)	Reference	χ
W	2	66	0.78 ± 0.32
Mo	5-25	66	0.88 ± 0.24
Nb	50	66	2.52 ± 0.85
Ta	35-50	66	3.84 ± 0.41
V	35-60	66	3.49 ± 1.77
Ti	16-37	66	1.22 ± 0.24
Zr	23-31,40-45	66	1.70 ± 0.31
Hf	25	66	1.68 ± 0.25
Re	25-28	68	0.85 ± 0.05
Mg	2-15	66,69	0.95 ± 0.08
Be	1-5	66,69	0.74 ± 0.13
Co	10-25	66	1.68 ± 0.13
Os	0	69	0.85 ± 0.06
Sc	1-8	67	1.16 ± 0.20
Ru	0	70	0.85 ± 0.07
Y	6-34	67	1.64 ± 0.34

C. Intrinsic Ductility of Alloys

The elastic stability, and intrinsic ductility, of a random solid solution alloy is determined by constructing SWT as a function of applied uniaxial strain along the known weakest direction of the crystal (see Methods II). To estimate the intrinsic ductility of Ta-Nb-V-W-Mo, Hf-Zr-Ti-Nb-V, Ta-Nb-V-W, and Ti-Ta-Nb-V the SOECs and TOECs for the alloys were computed by utilizing the SSOS method to compute SOECs and TOECs (see for VIB for computational details), though any electronic structure method suitable for computing elastic constants of alloys could be used. (See VIC for the computed values the SOECs and TOECs.) The resulting eigenvalues of SWT as a function of applied strain in tension

TABLE IV. Displaying the results of standard error and mean predicted 95% confidence interval of elongation to failure from linear model. All numbers are in % elongation.

System	Observed Elongation	Predicted Elongation	Standard Error	Confidence Interval
W	2	8.5	3.1	1.8 – 15.2
Mo	15.0	9.8	3.0	3.4 – 16.2
Nb	50.0	33.2	3.3	26.2 – 40.2
Ta	42.5	53.8	6.3	40.4 – 67.3
V	47.5	48.7	5.5	37.0 – 60.4
Ti	26.5	25.0	2.5	19.6 – 30.4
Zr	34.8	21.5	2.4	16.4 – 26.7
Hf	25.0	21.3	2.4	16.1 – 26.4
Re	26.5	9.2	3.0	2.7 – 15.7
Mg	8.5	10.6	2.9	4.4 – 16.8
Be	3.0	7.6	3.2	0.7 – 14.5
Co	17.5	21.3	2.4	16.1 – 26.4
Os	0	9.2	3.0	2.7 – 15.7
Sc	4.5	13.7	2.6	8.0 – 19.3
Ru	0	9.2	3.0	2.7 – 15.7
Y	20.0	20.7	2.4	15.6 – 25.8

(uniaxial load applied along $\langle 001 \rangle$) are shown in Fig. 4. It should be noted that due to the high symmetry that still exists in the crystal when loading along the $\langle 001 \rangle$ axis only four unique eigenvalues need to be considered. Experimental compression loading is considered for these alloy systems as a judge of ductility, as there is no experimental data available for elongations to failure under tension.

It should be noted that we also attempted to apply our model to estimating χ for the alloys under consideration in compression, as this would be ideal for comparing our model to the available experimental evidence. In this case, uniaxial compression along the $\langle 110 \rangle$ axis was applied, as this is thought to be the weakest loading axis under compression for BCC metals.⁴³ Uniaxial loading under $\langle 110 \rangle$ results in a strain state represented in Voigt

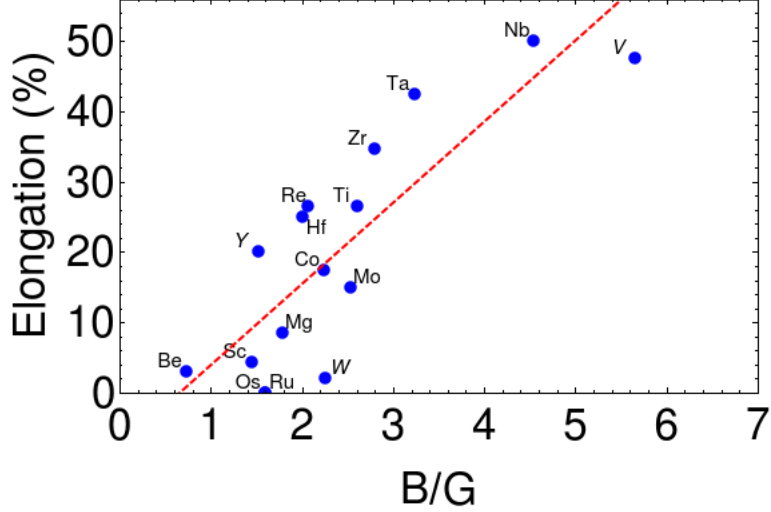
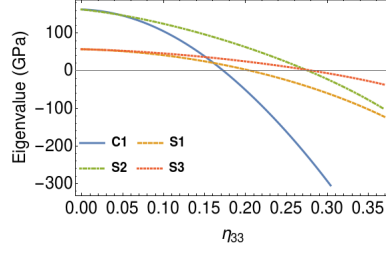


FIG. 3. Plot of Pugh ratio vs. elongation to fracture. The position of the points on the y-axis refers to their mean elongation to fracture.

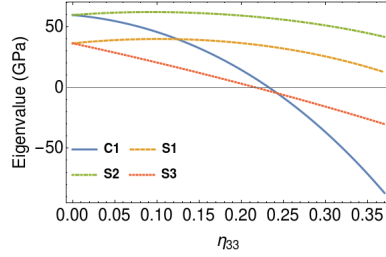
notation as $\boldsymbol{\eta} = (\eta_{11}, \eta_{22}, \xi, 0, 0, 0)$. As a condition of uniaxial loading is that $\sigma_{11} = 0$ and $\sigma_{22} = 0$, η_{11} and η_{22} can be determined as a function of ξ . Under uniaxial compression along $\langle 110 \rangle$ the alloys considered appear to reach instability at high strains ($\xi > 20\%$). This is problematic, because the derived relations for $\eta_{11} = \eta_{11}(\xi)$ and $\eta_{22} = \eta_{22}(\xi)$ have no solution at strains greater than $\xi \approx 10 - 20\%$, displaying one limitation to the method described in this work. As a result, only χ values for the alloys loaded in tension will be shown.

Our model predicts Ta-Nb-V-W-Mo fails in a brittle manner (the Young's modulus goes to zero) at approximately 16% strain in tension with $\chi = 0.60$. The calculation is in agreement with the brittle behavior (compression to fracture of 1.7% engineering strain) observed experimentally.²⁶ This implies elongations to failure less than those observed for W, and comparable to that of Os, which is known to be extremely brittle.⁶⁹ In the case of tension the linear model, generated from the elemental data, predicts an elongation to fracture of 5.6% with the 95% confidence bands for mean prediction being 0 – 13%.

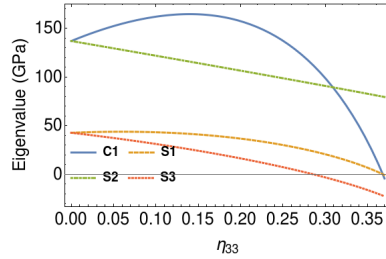
The same approach shows that Hf-Zr-Ti-Nb-V reaches elastic instability via a shear instability tension at 22% as shown in Fig. 4b. $\chi = 1.07$, indicating that a shear instability is encountered before the cleavage instability for the given loading condition. This suggests elongations to failure larger than those of Mo. In the case of tension the linear model generated from the elemental data predicts an elongation to fracture of 12% with the 95% confidence bands for mean prediction being 7 – 18%. A value of $\chi \approx 1$ does not necessarily



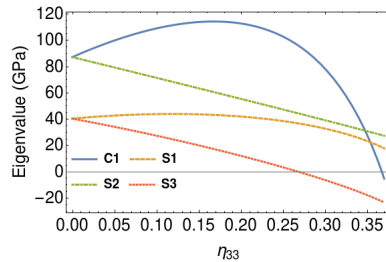
(a)



(b)



(c)



(d)

FIG. 4. Eigenvalues of the symmetric Wallace tensor for the four alloys considered in this work. Fig. 4a, 4b, 4c, 4d represent Ta-Nb-V-W-Mo, Hf-Zr-Ti-Nb-V, Ta-Nb-V-W, and Ti-Ta-Nb-V respectively. An eigenvalue less than or equal to zero corresponds to elastic instability. In the legend C corresponds to cleavage (or brittle) failure and S corresponds to shear failure. The numbers in the legend label the individual modes associated with ductile or brittle failure.

disagree with the findings of Li *et al.*'s ideal tensile strength calculations of Hf-Zr-Ti-Nb-V using CPA, which found the material to fail elastically at approximately 12% strain via

cleavage (which, for the approach used here, implies $\chi < 1$).³⁴

In the case of the four component alloys Ti-Ta-Nb-V is found to have a χ value of 1.38, which is the highest of the four alloys considered in this work, and corresponds to by far the most ductile behavior of the alloys considered (compression to failure of $> 40\%$). Ta-Nb-V-W has a predicted χ value of 1.29, which does not exactly agree with experimental findings of a compression to failure of 14%. This highlights that this χ parameter is not considered a quantitative predictor of ductility. Instead it is seen as a qualitative indicator of the relative ductilities of alloys.

As was done earlier in the case of the elemental systems it is worthwhile to compare the results of the χ calculations to that of the Pugh ratio. The Pugh ratio of the four equiatomic alloys was calculated using the isotropic bulk and shear modulus estimated using self-consistent bounds from the anisotropic elastic constants calculated using SSOS (Table VI). The Pugh ratios for Hf-Zr-Ti-Nb-V, Ta-Nb-V-W-Mo, Ta-Nb-V-W, and Ti-Ta-Nb-V are 3.4, 3.2, 4.0, and 3.9 respectively (as shown in Table VI). Thus, the Pugh ratio predicts that all of these equiatomic alloys should be highly ductile; all four systems would be predicted to have a similar ductility to Nb (it is helpful to compare these results Fig. 3). This prediction obviously does not concur with the experimental evidence shown in Table IV. While one must be careful in reading too much into the results from these four systems, in the case of these systems the χ parameter appears to be a much better predictor of ductility than the Pugh ratio.

TABLE V. Displaying the results of standard error and mean predicted 95% confidence interval of elongation to failure from linear model.

System	χ	Observed Compression (%)	Predicted Elongation (%)	Confidence Interval (%)
Ta-Nb-V-W-Mo	0.60	1.7 ²⁶	5.6	0-13.0
Hf-Zr-Ti-Nb-V	1.07	30 ⁵⁶	12.4	6.5-18.0
Ta-Nb-V-W	1.29	14 ⁵⁷	15.6	10.2-21.0
Ti-Ta-Nb-V	1.38	> 40 ⁵⁷	16.8	11.6-22.1

The intrinsic ductility parameter is now used to explore the influence of deviations in composition on the intrinsic ductility of Ta-Nb-V-W-Mo. Ta-Nb-V-W-Mo is of practical interest due to the high melting temperature of its constitutive elements.^{26,72} This alloy

shows good ductility (strains of 7.5 – 19% under compression) at high temperatures (1073 - 1473 K),⁷³ but the brittleness of the alloy at room temperature limits its applications. Based on the observation that Nb additions are expected to increase the ductility of Mo,^{40,74} it is interesting to explore the replacement of Mo with Nb to create the quaternary alloy $\text{Ta}_{0.2}\text{Nb}_{0.4}\text{V}_{0.2}\text{W}_{0.2}$. Nb is also an attractive replacement for Mo considering that the melting temperatures of the two elements are 2741 and 2895 K respectively.⁶⁶ The computed elastic constants (see VIC) predict a highly ductile alloy with $\chi = 2.21$ (for tensile loading), which is approximately the same value as that found for Nb (see Fig. 2). The linear model generated from the elemental data predicts an elongation to fracture of 29 % with the 95% confidence bands for mean prediction being 23 – 35%. This should be compared to $\chi = 0.60$ for the Ta-Nb-V-W-Mo alloy.

IV. DISCUSSION

It is likely that replacing Mo with Nb will still yield a single-phase BCC alloy considering that both the atomic size difference and valence electron concentration (VEC), two parameters often used to assess the phase stability of HEAs, hardly change. VEC would be reduced from 3.4 to 3.2 e^-/atom , while the atomic size difference⁷⁵ (calculated using the formula $\delta = \sqrt{\sum_{i=1}^N c_i(1 - r_i/\bar{r})^2}$, with N being the number of elements, c_i and r_i the concentration and atomic radius of the i^{th} element, obtained from reference,⁷⁶ and \bar{r} the average atomic radius) would go from 3.7% to 3.9%, which is within the empirically determined range of single phase stability.⁷⁷ Even if this specific alloy does not exist as a single phase, its high ductility strongly suggests that manipulating the relative concentrations of Mo and Nb in the alloy could be a successful strategy in increasing the ductility of the alloy, without greatly reducing the melting temperature.

The benchmarking calculations done for both elemental metals and high entropy alloys suggest that the calculation of SOECs and TOECs using the SSOS method, in concert with a nonlinear elasticity model for SWT, can be used effectively to order the intrinsic ductility of real systems. While it is true that direct ideal tensile strength calculations could be carried out with the SSOS method, these calculations would require a great deal more computational resources than the current approach. For instance, to calculate the ideal tensile strength of a BCC alloy, the strain path for a uniaxial load applied along

the [100], [010], and [001] direction must be computed. Then, the elastic constants as a function of strain for each of these strain paths must be computed, and then averaged to estimate the ideal strength. Moreover, to understand the details of the controlling elastic instability, one needs to compute SWT at (or very near) to the instabilities. This requires the computation of the elastic constants at each instability. For a general tensile direction in a cubic material, the problem increases in complexity. A nominally BCC compositionally complex alloy would require 24 different ideal tensile strength computations. Similarly, a direct ideal shear strength calculation would entail a much higher cost. The determination of the ideal shear strength for a load in the $\{\bar{1}\bar{1}2\}\langle 111\rangle$ orientation would require calculating the strain path for all 12 symmetrically equivalent orientations. This is in direct contrast to the nonlinear elasticity estimate of the SWT, which only requires the second- and third-order elastic constants to construct an ideal yield surface associated with an arbitrary loading configuration. This could enable the calculation of other ideal-strength-based estimations of mechanical properties, such as the ratio of the ideal tensile and shear strengths, which is shown to correlate with toughness.^{31,65}

Based on the comparison of χ with the measured elongation of commercially-pure metals and compression of refractory high-entropy alloys, we believe that this simple model has great potential as a tool for computer-aided materials design. Ductility is one of the most basic and important metrics used in evaluating a structural material, and the ability to assess it from first principles can do much to accelerate the design of structural materials.

It is noted, however, that materials may fail by a phonon instability, which will not be captured by SWT if the soft phonon is not near the Γ -point. This is a common mode of instability in face-centered cubic (FCC) metals.^{78,79} As a result, FCC metals have not been included in the benchmark calculations presented here. Note, however, that the calculation of χ is not relegated to the nonlinear elasticity model presented in this work, but can be used in any ideal strength calculation, as χ is defined as the ratio of strains at which cleavage and shear instabilities first occur (be they elastic or dynamical instabilities).

V. CONCLUSION

An intrinsic ductility parameter, that can be calculated from first principles, is introduced and appears to show good qualitative correlation with the experimentally measured elon-

gation to fracture of a range of elemental body-centered-cubic and hexagonal close-packed metals. It is shown how this intrinsic ductility parameter can be applied to alloys through the application of the small set of ordered structures model. Further, the intrinsic ductility parameter is utilized to predict a path for increasing the ductility of the refractory high-entropy alloy Ta-Nb-V-W-Mo, while maintaining its high melting temperature.

ACKNOWLEDGMENTS

This work was funded by the U.S. Department of Energy, Office of Science, Office of Basic Energy Sciences, Materials Sciences and Engineering Division under Contract No. DE-AC02-05-CH11231 (Materials Project program KC23MP). E. R. acknowledges support from the U.S. Office of Naval Research under grant N00014-16-1-2304. ISW's work was performed in part under the auspices of the U.S. Department of Energy by Lawrence Livermore National Laboratory under Contract DE-AC52-07NA27344.

VI. APPENDIX

A. Derivation of Strain Derivatives

This appendix shows how equation (8) can be derived such that $\frac{\partial \bar{\eta}_{pq}}{\beta_{ij}}$ and $\frac{\partial^2 \bar{\eta}_{mn}}{\beta_{ij}\beta_{kl}}$ are defined explicitly in terms of $\boldsymbol{\eta}$ and $\boldsymbol{\eta}$ only. The derivation begins by noting that the chain rule on $\bar{\mathbf{F}}$ such that

$$\bar{F}_{ij} = \frac{\partial \bar{x}_i}{\partial X_j} = \frac{\partial \bar{x}_i}{\partial x_k} \frac{\partial x_k}{\partial X_j} = f_{ik} F_{kj}. \quad (13)$$

Taking the definition of the Lagrangian strain, $\bar{\boldsymbol{\eta}}$, to be

$$2\bar{\boldsymbol{\eta}} = \bar{\mathbf{F}}^T \cdot \bar{\mathbf{F}} - \mathbf{I}, \quad (14)$$

with T representing the transpose of a given matrix, and substituting (13) into (14) results in

$$2\bar{\boldsymbol{\eta}} = (\mathbf{f} \cdot \mathbf{F})^T \cdot (\mathbf{f} \cdot \mathbf{F}) - \mathbf{I} \quad (15a)$$

$$2\bar{\boldsymbol{\eta}} = \mathbf{F}^T \cdot \mathbf{f}^T \cdot \mathbf{f} \cdot \mathbf{F} - \mathbf{I}. \quad (15b)$$

where \mathbf{I} is the identity. Because \mathbf{f} is within the linear elastic regime, it can be expressed as

$$\mathbf{f} = \mathbf{I} + \boldsymbol{\beta}, \quad (16)$$

with $\boldsymbol{\beta}$ being the infinitesimal strain, this means that \mathbf{f} is a symmetric tensor and as a result the $\bar{\boldsymbol{\eta}}$ can be written as

$$2\bar{\boldsymbol{\eta}} = \mathbf{F}^T \cdot (\mathbf{I} + \boldsymbol{\beta}) \cdot (\mathbf{I} + \boldsymbol{\beta}) \cdot \mathbf{F} - \mathbf{I}, \quad (17a)$$

$$2\bar{\boldsymbol{\eta}} = \mathbf{F}^T \cdot (\mathbf{I} \cdot \mathbf{I} + \mathbf{I} \cdot \boldsymbol{\beta} + \boldsymbol{\beta} \cdot \mathbf{I} + \boldsymbol{\beta} \cdot \boldsymbol{\beta}) \cdot \mathbf{F} - \mathbf{I}, \quad (17b)$$

$$2\bar{\boldsymbol{\eta}} = \mathbf{F}^T \cdot (\mathbf{I} + 2\boldsymbol{\beta} + \boldsymbol{\beta} \cdot \boldsymbol{\beta}) \cdot \mathbf{F} - \mathbf{I}. \quad (17c)$$

Using index notation equation (17c) is expressed as

$$2\bar{\eta}_{ij} = F_{ki} (\delta_{km} + 2\beta_{km} + \beta_{kn}\beta_{nm}) F_{mj} - \delta_{ij}. \quad (18)$$

As described in section II B, \mathbf{F} is not a function of $\boldsymbol{\beta}$. As such the first derivative of $\boldsymbol{\eta}$ with respect to $\boldsymbol{\beta}$ can be taken quite easily using equation (18):

$$\frac{\partial \bar{\eta}_{ij}}{\partial \beta_{pq}} = \frac{1}{2} F_{ki} F_{mj} \left(2 \frac{\partial \beta_{km}}{\partial \beta_{pq}} + \beta_{kn} \frac{\partial \beta_{nm}}{\partial \beta_{pq}} + \beta_{nm} \frac{\partial \beta_{kn}}{\partial \beta_{pq}} \right). \quad (19)$$

$\boldsymbol{\beta}$ is a symmetric tensor, meaning that

$$\frac{\partial \beta_{km}}{\partial \beta_{pq}} = I_{kmpq} = \frac{1}{2} (\delta_{kp}\delta_{mq} + \delta_{kq}\delta_{mp}), \quad (20)$$

where I_{kmpq} is the fourth rank identity tensor. If the first derivative of $\bar{\boldsymbol{\eta}}$ is evaluated at $\boldsymbol{\beta} = 0$, then

$$\left(\frac{\partial \bar{\eta}_{ij}}{\partial \beta_{pq}} \right)_{\bar{\boldsymbol{\eta}}=\boldsymbol{\eta}} = F_{ki} F_{mj} I_{kmpq}. \quad (21)$$

To calculate $\frac{\partial^2 \bar{\eta}_{mn}}{\partial \beta_{ij} \partial \beta_{kl}}$ it is helpful to substitute the symmetric fourth-rank identity tensor into equation (20), giving:

$$\frac{\partial \bar{\eta}_{ij}}{\partial \beta_{pq}} = \frac{1}{2} F_{ki} F_{mj} (2I_{kmpq} + \beta_{kn} I_{nmpq} + \beta_{nm} I_{knpq}). \quad (22)$$

Taking the second derivative with respect to $\boldsymbol{\beta}$ results in:

$$\frac{\partial^2 \bar{\eta}_{ij}}{\partial \beta_{pq} \partial \beta_{rs}} = \frac{1}{2} F_{ki} F_{mj} (I_{knrs} I_{nmpq} + I_{nmrs} I_{knpq}), \quad (23)$$

which is only dependent on \mathbf{F} . \mathbf{F} and $\boldsymbol{\eta}$ can be related to each other as described in II.

B. Computational Details

Elastic constants calculations were performed using DFT as implemented in the Vienna *Ab initio* Simulation Package^{80,81}. The Perdew, Burke, and Ernzerhof Generalized Gradient Approximation exchange-correlation functional was employed⁸². A plane-wave cutoff of 600 eV was used with a first-order Methfessel-Paxton smearing⁸³ employing a smearing parameter of 0.05 eV. Ionic relaxations were performed until all forces were less than 5 meV/Å. The total energy was converged to within 10^{-8} eV. For the equiatomic 5-component alloys elastic constants $10 \times 10 \times 40$, $16 \times 16 \times 16$, and $11 \times 11 \times 28$ Γ -centered k-point meshes were employed for the first, second, and third SQS respectively. For the equiatomic 4-component alloys elastic constants $20 \times 20 \times 20$, $24 \times 24 \times 12$, $18 \times 18 \times 25$, and $20 \times 20 \times 20$ Γ -centered k-point meshes were employed for the first, second, third, and fourth SQS respectively. The SOEC and TOEC were calculated following the approaches outlined by de Jong *et al.*^{44,51}. The k-point meshes used for the Ta_{0.2}Nb_{0.4}V_{0.2}W_{0.2} alloy were: $16 \times 16 \times 16$ Γ -centered for the first, second, and fourth SSOS; and $12 \times 12 \times 30$ Γ -centered for the third SSOS.

C. Elastic Constants of Alloys

The SOECs and TOECs were calculated following the approach outlined by de Jong *et al.*^{44,51}. The method for determining the TOECs works by applying a number of different strain states written in terms of the strain parameter, η , applying a finite difference approach to find the second derivative of the second Piola-Kirchhoff stress values and then using pseudoinversion to determine the TOEC. It was found that instead of the 21 strain states used to approximate the TOECs in reference⁴⁴, only 14 are needed to completely determine

the 56 unique TOECs of an unsymmetrized crystal. The 14 unique strains are listed using Voigt notation as

$$\boldsymbol{\eta}^1 = \begin{pmatrix} \eta & 0 & 0 & 0 & 0 & 0 \end{pmatrix}, \quad (24a)$$

$$\boldsymbol{\eta}^2 = \begin{pmatrix} 0 & \eta & 0 & 0 & 0 & 0 \end{pmatrix}, \quad (24b)$$

$$\boldsymbol{\eta}^3 = \begin{pmatrix} 0 & 0 & \eta & 0 & 0 & 0 \end{pmatrix}, \quad (24c)$$

$$\boldsymbol{\eta}^4 = \begin{pmatrix} 0 & 0 & 0 & 2\eta & 0 & 0 \end{pmatrix}, \quad (24d)$$

$$\boldsymbol{\eta}^5 = \begin{pmatrix} 0 & 0 & 0 & 0 & 2\eta & 0 \end{pmatrix}, \quad (24e)$$

$$\boldsymbol{\eta}^6 = \begin{pmatrix} 0 & 0 & 0 & 0 & 0 & 2\eta \end{pmatrix}, \quad (24f)$$

$$\boldsymbol{\eta}^7 = \begin{pmatrix} \eta & \eta & 0 & 0 & 0 & 0 \end{pmatrix}, \quad (24g)$$

$$\boldsymbol{\eta}^8 = \begin{pmatrix} \eta & 0 & \eta & 0 & 0 & 0 \end{pmatrix}, \quad (24h)$$

$$\boldsymbol{\eta}^9 = \begin{pmatrix} \eta & 0 & 0 & 2\eta & 0 & 0 \end{pmatrix}, \quad (24i)$$

$$\boldsymbol{\eta}^{10} = \begin{pmatrix} \eta & 0 & 0 & 0 & 2\eta & 0 \end{pmatrix}, \quad (24j)$$

$$\boldsymbol{\eta}^{11} = \begin{pmatrix} 0 & \eta & \eta & 0 & 0 & 0 \end{pmatrix}, \quad (24k)$$

$$\boldsymbol{\eta}^{12} = \begin{pmatrix} 0 & 0 & 0 & 2\eta & 2\eta & 0 \end{pmatrix}, \quad (24l)$$

$$\boldsymbol{\eta}^{13} = \begin{pmatrix} 0 & 0 & 0 & 2\eta & 0 & 2\eta \end{pmatrix}, \quad (24m)$$

$$\boldsymbol{\eta}^{14} = \begin{pmatrix} 0 & 0 & 0 & 0 & 2\eta & 2\eta \end{pmatrix}. \quad (24n)$$

D. Special Quasirandom Structures

In Tables VIII and IX the SQS cells used for calculating the elastic constants of the 4-component equiatomic alloys and $\text{Ta}_{0.2}\text{Nb}_{0.4}\text{V}_{0.2}\text{W}_{0.2}$ are displayed.

E. Assessment of Crystallinity

In order to ensure that the SQS cells considered in this work remained BCC after structural relaxation, adaptive common neighbor analysis (a-cna) was applied to all relaxed cells⁸⁴ using the open visualization tool (OVITO)^{85,86}. In the case of Ta-Nb-V-W-Mo all three cells

TABLE VI. List of the SOECs (and the isotropic Pugh ratio: B/G) for all SQS of the two HEA considered in this study plus the ductile alloy $\text{Ta}_{0.2}\text{Nb}_{0.4}\text{V}_{0.2}\text{W}_{0.2}$. The numbering of each compound corresponds to its rank with respect to approximating a random solution. All elastic constants values are in units of GPa.

SSOS	C_{11}	C_{12}	C_{44}	B/G
Hf-Zr-Ti-Nb-V				
(1)	153	94.4	32.0	
(2)	167	89.6	36.7	
(3)	145	103	38.0	
(weighted average)	156	96.0	36.3	3.4
Ta-Nb-V-W-Mo				
(1)	340	156	65.6	
(2)	331	159	54.0	
(3)	325	164	56.2	
(weighted average)	331	160	57.2	3.2
Ta-Nb-V-W				
(1)	308	159	50.0	
(2)	290	164	34.4	
(3)	301	160	45.7	
(4)	308	157	54.5	
(weighted average)	298	161	42.6	4.0
Ti-Ta-Nb-V				
(1)	202	134	27.3	
(2)	213	127	44.3	
(3)	220	129	40.8	
(4)	221	126	35.0	
(weighted average)	215	129	40.1	3.9
$\text{Ta}_{0.2}\text{Nb}_{0.4}\text{V}_{0.2}\text{W}_{0.2}$				
(1)	340	119	29.4	
(2)	275	155	35.3	
(3)	288	154	43.7	
(4)	296	150	44.0	

TABLE VII. List of the TOECs for all SQS of the HEA considered in this study. The numbering of each compound corresponds to its rank with respect to approximating a random solution. All elastic constants values are in units of GPa.

SSOS	C_{111}	C_{112}	C_{123}	C_{144}	C_{166}	C_{456}
Hf-Zr-Ti-Nb-V						
(1)	-1460	-327	-135	-208	-164	-120
(2)	-1180	-393	-195	-229	-173	-59.3
(3)	-1350	-366	-167	-229	-204	50.1
(weighted average)	-1310	-369	-172	-225	-184	-27.7
Ta-Nb-V-W-Mo						
(1)	-3030	-770	-36.8	-404	-519	-512
(2)	-3760	-574	-230	-328	-482	-521
(3)	-3410	-767	78.6	-334	-568	-478
(weighted average)	-3480	-691	-68.0	-345	-524	-502
Ta-Nb-V-W						
(1)	-1490	-791	-766	-321	-363	185
(2)	-1430	-808	-490	-230	-379	-143
(3)	-1710	-807	-654	-328	-406	-50.1
(4)	-1710	-821	-859	-415	-340	-61.7
(weighted average)	-1570	-807	-622	-297	-383	-63.8
Ti-Ta-Nb-V						
(1)	-1610	-924	-631	-436	-566	110
(2)	-1320	-710	-412	-272	-225	129
(3)	-895	-575	-373	-158	-263	-44.5
(4)	-1390	-490	-679	-241	-86.6	-10.2
(weighted average)	-1200	-659	-451	-244	-260	46.8
$Ta_{0.2}Nb_{0.4}V_{0.2}W_{0.2}$						
(1)	-2970	-278	-607	-740	-739	257
(2)	-1820	-1140	180	-329	-294	47.9
(3)	-1710	-711	-806	-342	-336	151
(4)	-1740	-887	-489	-360	-314	111
(weighted average)	-1950	-816	-438	-414	-395	113

TABLE VIII. Definition of SQS cells used for calculating the elastic constants of Ta-Nb-V-W and Ti-Ta-Nb-V.

SQS	a_0 (Å)	Lattice Vectors (a_0)	Atomic Positions
1	Ta-Nb-V-W: 3.20	$\mathbf{a} = (0.0, 1.0, 1.0)$	atom 1 - (0.75, 0.75, 0.75)
			atom 2 - (0.50, 0.50, 0.50)
	Ti-Ta-Nb-V: 3.22	$\mathbf{b} = (1.0, 0.0, 1.0)$	atom 3 - (0.00, 0.00, 0.00)
			$\mathbf{c} = (1.0, 1.0, 0.0)$
2	Ta-Nb-V-W: 3.20	$\mathbf{a} = (-1.0, 0.0, 0.0)$	atom 1 - (0.50, 0.50, 0.75)
			atom 2 - (0.00, 0.00, 0.00)
	Ti-Ta-Nb-V: 3.23	$\mathbf{b} = (0.0, 0.0, 1.0)$	atom 3 - (0.00, 0.00, 0.50)
			$\mathbf{c} = (0.0, 2.0, 0.0)$
3	Ta-Nb-V-W: 3.21	$\mathbf{a} = (0.0, -1.0, 1.0)$	atom 1 - (0.00, 0.00, 0.00)
			atom 2 - (0.00, 0.50, 0.50)
	Ti-Ta-Nb-V: 3.22	$\mathbf{b} = (0.0, 1.0, 1.0)$	atom 3 - (0.50, 0.00, 0.50)
			$\mathbf{c} = (-1.0, 0.0, 0.0)$
4	Ta-Nb-V-W: 3.21	$\mathbf{a} = (0.5, 0.5, 1.5)$	atom 1 - (0.75, 0.25, 0.50)
			atom 2 - (0.50, 0.50, 0.00)
	Ti-Ta-Nb-V: 3.22	$\mathbf{b} = (-0.5, 1.5, 0.5)$	atom 3 - (0.25, 0.75, 0.50)
			$\mathbf{c} = (-0.5, -1.5, 0.5)$

were found to be 100% BCC. The second and third SQS were determined to be completely BCC for Hf-Zr-Ti-Nb-V, but the first SQS was 80% BCC. To test if this large relaxation had an effect on the results presented in this paper, the first SQS was excluded from the calculation of the symmetrized elastic constants. This resulted in the failure strains being $\xi_S = 21.9\%$, $\xi_C = 25.7\%$, and $\chi = 1.17$ as compared to $\xi_S = 21.7\%$, $\xi_C = 23.2\%$, and $\chi = 1.07$ when all three structures were considered. All cells considered for the two 4-component equiatomic alloys and $\text{Ta}_{0.2}\text{Nb}_{0.4}\text{V}_{0.2}\text{W}_{0.2}$ system were found to be BCC.

* ian.winter@berkeley.edu

TABLE IX. Definition of SQS cells used for calculating the elastic constants of $\text{Ta}_{0.2}\text{Nb}_{0.4}\text{V}_{0.2}\text{W}_{0.2}$.

SQS	a_0 (Å)	Lattice Vectors (a_0)	Atomic Positions
1	3.22	$\mathbf{a} = (-0.5, 2.5, -0.5)$ $\mathbf{b} = (0.5, 2.5, 0.5)$ $\mathbf{c} = (0.5, -2.5, -0.5)$	Nb - (0.4, 0.4, 0.0)
			Nb - (0.8, 0.8, 0.0)
			Ta - (0.0, 0.0, 0.0)
			V - (0.6, 0.6, 0.0)
			W - (0.2, 0.2, 0.0)
2	3.23	$\mathbf{a} = (-0.5, -1.5, -0.5)$ $\mathbf{b} = (-0.5, 1.5, 0.5)$ $\mathbf{c} = (0.5, 0.5, -1.5)$	Nb - (0.8, 0.4, 0.2)
			Nb - (0.2, 0.6, 0.8)
			Ta - (0.6, 0.8, 0.4)
			V - (0.4, 0.2, 0.6)
			W - (0.0, 0.0, 0.0)
3	3.23	$\mathbf{a} = (-0.5, -1.5, -1.5)$ $\mathbf{b} = (-1.5, -0.5, -1.5)$ $\mathbf{c} = (0.5, 0.5, -0.5)$	Nb - (0.8, 0.8, 0.2)
			Nb - (0.2, 0.2, 0.8)
			Ta - (0.6, 0.6, 0.4)
			V - (0.0, 0.0, 0.0)
			W - (0.4, 0.4, 0.6)
4	3.22	$\mathbf{a} = (-1.5, 0.5, 0.5)$ $\mathbf{b} = (-0.5, 0.5, 1.5)$ $\mathbf{c} = (-0.5, 1.5, 0.5)$	Nb - (0.4, 0.4, 0.4)
			Nb - (0.6, 0.6, 0.6)
			Ta - (0.0, 0.0, 0.0)
			V - (0.8, 0.8, 0.8)
			W - (0.2, 0.2, 0.2)

† dcchrzan@berkeley.edu

¹ J. Pokluda and P. Šandera, [Micromechanisms of Fracture and Fatigue: In a Multiscale Context](#) (Springer, 2010).

² D. Roundy, C. R. Krenn, M. L. Cohen, and J. W. Morris, [Phys. Rev. Lett.](#) **82**, 2713 (1999).

³ S. Ogata, J. Li, and S. Yip, [Science](#) **298**, 807 (2002).

⁴ S. G. Corcoran, R. J. Colton, E. T. Lilleodden, and W. W. Gerberich, [Phys. Rev. B](#) **55**, R16057 (1997).

- ⁵ M. M. Biener, J. Biener, A. M. Hodge, and A. V. Hamza, *Phys. Rev. B* **76**, 165422 (2007).
- ⁶ C. A. Schuh, J. K. Mason, and A. C. Lund, *Nat. Mater.* **4**, 617 (2005).
- ⁷ C. A. Schuh, *Mater. Today* **9**, 32 (2006).
- ⁸ J. R. Morris, H. Bei, G. M. Pharr, and E. P. George, *Phys. Rev. Lett.* **106**, 165502 (2011).
- ⁹ D. Bahr, D. Kramer, and W. Gerberich, *Acta Mater.* **46**, 3605 (1998).
- ¹⁰ C. Woodcock and D. Bahr, *Scr. Mater.* **43**, 783 (2000).
- ¹¹ J. Li, K. J. Van Vliet, T. Zhu, S. Yip, and S. Suresh, *Nature* **418**, 307 (2002).
- ¹² R. Hill and F. Milstein, *Phys. Rev. B* **15**, 3087 (1977).
- ¹³ F. Milstein and B. Farber, *Phys. Rev. Lett.* **44**, 277 (1980).
- ¹⁴ N. Nagasako, M. Jahnátek, R. Asahi, and J. Hafner, *Phys. Rev. B* **81**, 94108 (2010).
- ¹⁵ T. Li, J. W. Morris, and D. C. Chrzan, *Phys. Rev. B* **70**, 054107 (2004).
- ¹⁶ J. Frenkel, *Zeitschrift für Physik* **37**, 572 (1926).
- ¹⁷ E. Orowan, *Zeitschrift für Physik* **89**, 605 (1934).
- ¹⁸ M. Polanyi, *Zeitschrift für Physik* **89**, 660 (1934).
- ¹⁹ G. I. Taylor, *Proceedings of the Royal Society of London A: Mathematical, Physical and Engineering Sciences* **145**, 362 (1934).
- ²⁰ H. Wang and M. Li, *Phys. Rev. Lett.* **111**, 065507 (2013).
- ²¹ B. Cantor, I. Chang, P. Knight, and A. Vincent, *Materials Science and Engineering: A* **375-377**, 213 (2004).
- ²² M.-H. Tsai and J.-W. Yeh, *Materials Research Letters* **2**, 107 (2014).
- ²³ D. Miracle and O. Senkov, *Acta Materialia* **122**, 448 (2017).
- ²⁴ Y. Zhang, T. T. Zuo, Z. Tang, M. C. Gao, K. A. Dahmen, P. K. Liaw, and Z. P. Lu, *Progress in Materials Science* **61**, 1 (2014).
- ²⁵ M.-H. Chuang, M.-H. Tsai, W.-R. Wang, S.-J. Lin, and J.-W. Yeh, *Acta Materialia* **59**, 6308 (2011).
- ²⁶ O. Senkov, G. Wilks, J. Scott, and D. Miracle, *Intermetallics* **19**, 698 (2011).
- ²⁷ Z. Li, K. G. Pradeep, Y. Deng, D. Raabe, and C. C. Tasan, *Nature* **534**, 227 (2016).
- ²⁸ D. B. Miracle, J. D. Miller, O. N. Senkov, C. Woodward, M. D. Uchic, and J. Tiley, *Entropy* **16**, 494 (2014).
- ²⁹ D. B. Miracle, *Materials Science and Technology* **31**, 1142 (2015).

- ³⁰ P. Singh, A. Sharma, A. V. Smirnov, M. S. Diallo, P. K. Ray, G. Balasubramanian, and D. D. Johnson, [npj Computational Materials](#) **4**, 16 (2018).
- ³¹ S. Ogata and J. Li, *Journal of Applied Physics* **106**, 113534 (2009).
- ³² T. Li, J. W. Morris, N. Nagasako, S. Kuramoto, and D. C. Chrzan, *Phys. Rev. Lett.* **98**, 105503 (2007).
- ³³ X. Li, S. Schönecker, J. Zhao, B. Johansson, and L. Vitos, *Phys. Rev. B* **87**, 214203 (2013).
- ³⁴ X. Li, F. Tian, S. Schönecker, J. Zhao, and L. Vitos, *Scientific reports* **5**, 12334 (2015).
- ³⁵ D. C. Wallace, *Thermodynamics of Crystals* (Courier Corporation, 1998).
- ³⁶ W. Morris Jr and C. R. Krenn, *Philos. Mag. A* **80**, 2827 (2000).
- ³⁷ H. Wang and M. Li, *Phys. Rev. B* **85**, 104103 (2012).
- ³⁸ F. Birch, *Phys. Rev.* **71**, 809 (1947).
- ³⁹ W. Luo, D. Roundy, M. L. Cohen, and J. W. Morris, *Phys. Rev. B* **66**, 094110 (2002).
- ⁴⁰ L. Qi and D. C. Chrzan, *Phys. Rev. Lett.* **112**, 115503 (2014).
- ⁴¹ D. Roundy, C. R. Krenn, M. L. Cohen, and J. W. Morris, *Philos. Mag. A* **81**, 1725 (2001).
- ⁴² F. Milstein, J. Marschall, and H. E. Fang, *Phys. Rev. Lett.* **74**, 2977 (1995).
- ⁴³ F. Milstein and S. Chantasiriwan, *Phys. Rev. B* **58**, 6006 (1998).
- ⁴⁴ M. de Jong, I. Winter, D. C. Chrzan, and M. Asta, *Phys. Rev. B* **96**, 014105 (2017).
- ⁴⁵ J. Tromp, M. L. Marcondes, R. M. M. Wentzcovitch, and J. Trampert, *Journal of Geophysical Research: Solid Earth* **124**, 729 (2019), <https://agupubs.onlinelibrary.wiley.com/doi/pdf/10.1029/2018JB016778>.
- ⁴⁶ S. P. Ong, W. D. Richards, A. Jain, G. Hautier, M. Kocher, S. Cholia, D. Gunter, V. L. Chevrier, K. A. Persson, and G. Ceder, *Computational Materials Science* **68**, 314 (2013).
- ⁴⁷ I. S. Winter, J. Montoya, K. A. Persson, and D. C. Chrzan, *Phys. Rev. Materials* **2**, 073601 (2018).
- ⁴⁸ A. Jain, S. P. Ong, G. Hautier, W. Chen, W. D. Richards, S. Dacek, S. Cholia, D. Gunter, D. Skinner, G. Ceder, et al., *Apl Materials* **1**, 011002 (2013).
- ⁴⁹ A. Zunger, S.-H. Wei, L. G. Ferreira, and J. E. Bernard, *Phys. Rev. Lett.* **65**, 353 (1990).
- ⁵⁰ S.-H. Wei, L. G. Ferreira, J. E. Bernard, and A. Zunger, *Phys. Rev. B* **42**, 9622 (1990).
- ⁵¹ M. de Jong, D. L. Olmsted, A. van de Walle, and M. Asta, *Phys. Rev. B* **86**, 224101 (2012).
- ⁵² C. Jiang and B. P. Uberuaga, *Phys. Rev. Lett.* **116**, 105501 (2016).
- ⁵³ A. van de Walle, M. Asta, and G. Ceder, *Calphad* **26**, 539 (2002).

- ⁵⁴ A. van de Walle, *Calphad* **33**, 266 (2009).
- ⁵⁵ A. van de Walle, P. Tiwary, M. De Jong, D. Olmsted, M. Asta, A. Dick, D. Shin, Y. Wang, L.-Q. Chen, and Z.-K. Liu, *Calphad* **42**, 13 (2013).
- ⁵⁶ E. Fazakas, V. Zadorozhnyy, L. Varga, A. Inoue, D. Louzguine-Luzgin, F. Tian, and L. Vitos, *International Journal of Refractory Metals and Hard Materials* **47**, 131 (2014).
- ⁵⁷ H. Yao, J. Qiao, J. Hawk, H. Zhou, M. Chen, and M. Gao, *Journal of Alloys and Compounds* **696**, 1139 (2017).
- ⁵⁸ B. Gairola and E. Kröner, *International Journal of Engineering Science* **19**, 865 (1981).
- ⁵⁹ C. M. Kube and M. de Jong, *Journal of Applied Physics* **120**, 165105 (2016).
- ⁶⁰ V. Lubarda, *Elastoplasticity Theory* (CRC Press, 2002).
- ⁶¹ J. Qu and M. Cherkaoui, *Fundamentals of micromechanics of solids* (Wiley Hoboken, 2006).
- ⁶² H. Song, F. Tian, Q.-M. Hu, L. Vitos, Y. Wang, J. Shen, and N. Chen, *Phys. Rev. Materials* **1**, 023404 (2017).
- ⁶³ L.-Y. Tian, L.-H. Ye, Q.-M. Hu, S. Lu, J. Zhao, and L. Vitos, *Computational Materials Science* **128**, 302 (2017).
- ⁶⁴ L.-Y. Tian, Q.-M. Hu, R. Yang, J. Zhao, B. Johansson, and L. Vitos, *Journal of Physics: Condensed Matter* **27**, 315702 (2015).
- ⁶⁵ S. Ogata, J. Li, N. Hirotsuki, Y. Shibutani, and S. Yip, *Phys. Rev. B* **70**, 104104 (2004).
- ⁶⁶ F. Cardarelli, *Materials handbook: a concise desktop reference* (Springer Science & Business Media, 2008).
- ⁶⁷ K. A. Gschneidner and L. Eyring, *Handbook on the Physics and Chemistry of Rare Earths*, Vol. 1 (Elsevier, 1978) pp. 1–894.
- ⁶⁸ C. T. Sims, C. M. Craighead, and R. I. Jaffee, *JOM* **7**, 168 (1955).
- ⁶⁹ S. Pugh, *The London, Edinburgh, and Dublin Philosophical Magazine and Journal of Science* **45**, 823 (1954).
- ⁷⁰ A. Darling, *Platinum Metals Review* **10**, 14 (1966).
- ⁷¹ W. R. Inc., “Mathematica, Version 11.3,” Champaign, IL, 2018.
- ⁷² O. Senkov, G. Wilks, D. Miracle, C. Chuang, and P. Liaw, *Intermetallics* **18**, 1758 (2010).
- ⁷³ O. Senkov, J. Scott, S. Senkova, D. Miracle, and C. Woodward, *Journal of Alloys and Compounds* **509**, 6043 (2011).

- ⁷⁴ S. Sheikh, S. Shafeie, Q. Hu, J. Ahlström, C. Persson, J. Veselý, J. Zýka, U. Klement, and S. Guo, *Journal of Applied Physics* **120**, 164902 (2016).
- ⁷⁵ S. Fang, X. Xiao, L. Xia, W. Li, and Y. Dong, *Journal of Non-Crystalline Solids* **321**, 120 (2003).
- ⁷⁶ C. Kittel, “Introduction to solid state physics,” (1980).
- ⁷⁷ Y. Zhang, Y. Zhou, J. Lin, G. Chen, and P. Liaw, *Advanced Engineering Materials* **10**, 534 (2008).
- ⁷⁸ D. M. Clatterbuck, C. R. Krenn, M. L. Cohen, and J. W. Morris, *Phys. Rev. Lett.* **91**, 135501 (2003).
- ⁷⁹ P. Řehák, M. Černý, and M. Šob, *Modelling and Simulation in Materials Science and Engineering* **23**, 055010 (2015).
- ⁸⁰ G. Kresse and J. Furthmüller, *Phys. Rev. B* **54**, 11169 (1996).
- ⁸¹ G. Kresse and J. Hafner, *Phys. Rev. B* **47**, 558 (1993).
- ⁸² J. P. Perdew, K. Burke, and M. Ernzerhof, *Phys. Rev. Lett.* **77**, 3865 (1996).
- ⁸³ M. Methfessel and A. T. Paxton, *Phys. Rev. B* **40**, 3616 (1989).
- ⁸⁴ A. Stukowski, *Modelling and Simulation in Materials Science and Engineering* **20**, 045021 (2012).
- ⁸⁵ A. Stukowski, *Modelling and Simulation in Materials Science and Engineering* **18**, 015012 (2010).
- ⁸⁶ “Ovito,” <http://ovito.org/>.